Direct Deposition of Crystalline Ta<sub>3</sub>N<sub>5</sub> Thin-Films on FTO for PEC Water Splitting

Hamed Hajibabaei<sup>a</sup>, Daniel J. Little<sup>a</sup>, Ayush Pandey<sup>d</sup>, Dunwei Wang<sup>b</sup>, Zetian Mi<sup>d</sup>, Thomas W.

Hamann<sup>a</sup>\*

<sup>a</sup> Department of Chemistry, Michigan State University, 578 S Shaw Lane East Lansing,

Michigan 48824-1322, USA

<sup>b</sup> Department of Chemistry, Merkert Chemistry Center, Boston College, 2609 Beacon Street,

Chestnut Hill, MA 02467, USA

<sup>d</sup> Department of Electrical Engineering and Computer Science, 1301 Beal Avenue, University

of Michigan, Ann Arbor, MI 48109, USA

\*hamann@chemistry.msu.edu

Keywords: ALD, CVD, Ta<sub>3</sub>N<sub>5</sub>, Tantalum Nitride, FTO, Photoanode, Water Splitting

**Abstract** 

Tantalum Nitride is a promising photoanode material for solar water splitting, but the further study

and practical use is constrained by the harsh conditions of the synthesis from Ta metal. Here we

report the direct deposition of crystalline Ta<sub>3</sub>N<sub>5</sub> on FTO substrate *via* a custom-built ALD system.

A combination of TaCl<sub>5</sub> (Ta-precursor) and ammonia (N-source) were sequentially pulsed into the

ALD reactor with the substrate heated to 550 °C to deposit compact and thin films of Ta<sub>3</sub>N<sub>5</sub> with

controllable thicknesses on FTO substrates. Importantly, it is shown that the FTO is chemically

and structurally stable under the reducing conditions of ammonia at 550 °C. These electrodes

produced an exceptional photocurrent onset potential of ~ 0.3 V vs. RHE with a maximum

photocurrent of ~ 2.4 mA cm<sup>-2</sup> at 1.23 V vs RHE. Results of photoelectrochemical investigations

as a function of film thickness and illumination direction reveal that the performance of Ta<sub>3</sub>N<sub>5</sub> is

controlled by a hole diffusion length of ~50 nm. These results are crucial for the successful

integration of Ta<sub>3</sub>N<sub>5</sub> in efficient unassisted water splitting applications.

1

#### Introduction

Tantalum nitride (Ta<sub>3</sub>N<sub>5</sub>) is one of the most promising semiconductor materials for photoelectrochemical (PEC) water oxidation. Several reports have shown that Ta<sub>3</sub>N<sub>5</sub> photoelectrodes are capable of producing a photocurrent approaching its theoretical band-gap limit of ~12.5 mA cm<sup>-2</sup>. <sup>1-4</sup> Despite this promising performance, the instability under PEC water oxidation conditions, low surface charge collection efficiency, and positive photocurrent onset potential with respect to its flat band potential limit the overall PEC water oxidation efficiency on Ta<sub>3</sub>N<sub>5</sub>. In order to improve the surface charge collection efficiency, the surface of photoelectrodes are commonly modified with a combination of water oxidation catalysts and hole storage layers. 1-<sup>3,5-8</sup> For example Li and coworkers<sup>2</sup> introduced the state-of-the-art Ta<sub>3</sub>N<sub>5</sub> photoanode by deposition of several successive layers - including a thin layer of TiO<sub>x</sub> as an electron blocking layer, FeOOH and Ni(OH)<sub>2</sub> as hole storage layers, and finally a layer of molecular catalyst to promote the kinetic of water oxidation reaction. The integrated electrode produced a photocurrent density of > 12.0 mA cm<sup>-2</sup> at water oxidation potential with a photocurrent onset potential of ~ 0.65 V vs. RHE. The instability of Ta<sub>3</sub>N<sub>5</sub> originates from the fast and irreversible surface photocorrosion forming surface tantalum oxide which results in a fast decay in the PEC performance. 6,9 Surface treatments such as doping, surface modifications with catalyst and surface protection layers have shown as effective strategies to circumvent this issue. 3,10,11 For example, Domen and coworkers<sup>10</sup> have recently shown that a combination of GaN as a protection layer and CoPi as the water oxidation catalyst stabilized the Ta<sub>3</sub>N<sub>5</sub> electrode under 10 h of continuous illuminations of water oxidation conditions, which to date is the most stable Ta<sub>3</sub>N<sub>5</sub> photoelectrode reported.

The synthesis of almost all of the high-performing Ta<sub>3</sub>N<sub>5</sub> electrodes reported to date start with the oxidation of a Ta-substrate *via* electrochemical anodization or by heating a Ta-substrate in air to oxidize the top Ta layer to produce nanostructured or planar tantalum oxide films, respectively. <sup>1,2,5,12–14</sup> The tantalum oxide samples are subsequently nitridized in a flow of ammonia at elevated temperatures (850 - 1000 °C) for a prolonged period of time (2 - 15 hours). The Ta-substrate serves as the source of Ta, the conductive layer to collect the majority charge carriers necessary to fabricate electrode, and the substrate. For example, Domen and coworkers<sup>1</sup> adopted a two-steps procedure of mask anodization followed by ammonolysis at 1000 °C for 2h to fabricate

a high aspect ratio films of undoped and Ba-doped Ta<sub>3</sub>N<sub>5</sub> on Ta substrate. The mask anodization resulted in a well-defined vertically oriented nanorods of Ta<sub>3</sub>N<sub>5</sub> with a 60 nm diameter and 600 nm length. These electrodes produced a photocurrent density of ~ 5 mA cm<sup>-2</sup> at the thermodynamic water oxidation potential. While this synthesis method is relatively simple and resulted in the best performing Ta<sub>3</sub>N<sub>5</sub> photoanodes, from the synthetic point of view there are multiple drawbacks: it is very energy intensive, produces a sizable quantity of chemical waste, results in the formation of electronically resistive phases at the Ta<sub>3</sub>N<sub>5</sub>|Ta junction limiting electron collection efficiency, Ta as a substrate becomes very brittle after heating in ammonia which makes the post-annealing electrode processing very challenging, Ta is not transparent, and this method provides a strongly reducing condition. The last two drawbacks are specifically important as they precludes the applicability of Ta<sub>3</sub>N<sub>5</sub> in the tandem cell configuration, i.e. the most efficient cell configuration for PEC water splitting systems. 15-17 Transparent conductive substrate is the indispensable part of a dual band gap tandem cell, creating electrical contact between a photoanode (top electrode) and a photocathode (bottom electrode) while having minimal light absorption in the visible to near IR region (Figure 1). The commercially available transparent conductive substrates are not stable under the high-temperature ammonolysis conditions utilized for synthesis of Ta<sub>3</sub>N<sub>5</sub>. As a result, Ta or noble metals like Pt<sup>5,13</sup> which indeed are not transparent to the Ta<sub>3</sub>N<sub>5</sub> sub-bandgap photons are the most viable substrates, to date. The known examples of transparent Ta<sub>3</sub>N<sub>5</sub> photoanodes are only limited to special transparent conductive substrates such as Ta-doped TiO2 and n-type GaN which are stable under highly reactive synthesis conditions of Ta<sub>3</sub>N<sub>5</sub>. 15,18

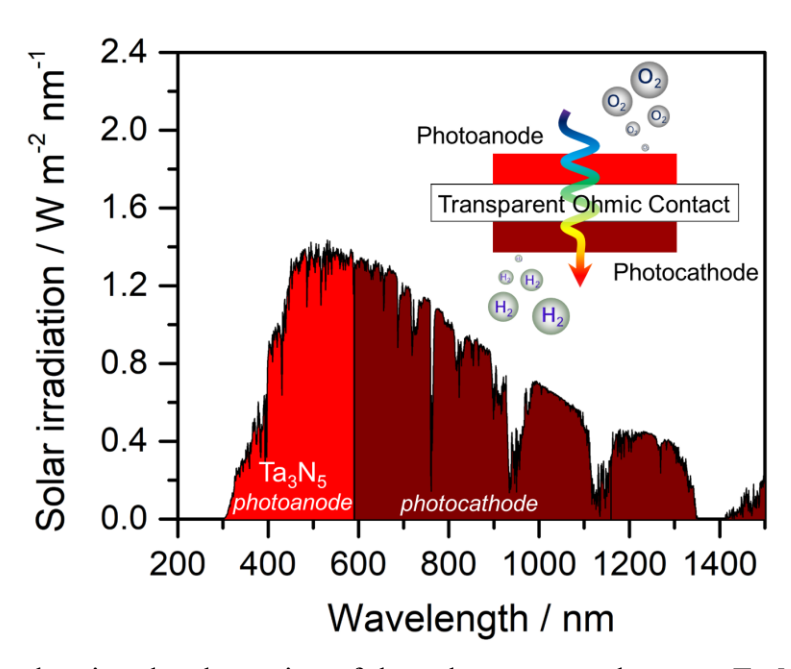


**Figure 1.** Scheme showing the absorption of the solar spectrum by a top Ta<sub>3</sub>N<sub>5</sub> photoanode and the transmitted light available for a bottom photocathode. Growth of Ta<sub>3</sub>N<sub>5</sub> on such transparent substrates is critical to allow such a tandem PEC water splitting cell to achieve efficient unassisted water splitting.

Jaramillo *et al.*<sup>12</sup> studied the structure and phase transformation of tantalum oxide to tantalum nitride films on various substrates including Ta foil and fused silica. They showed that the films on fused silica were single phase Ta<sub>3</sub>N<sub>5</sub>, but that the films prepared on Ta substrates were comprised of impurity phases, and upon rising the ammonolysis temperature, the formation of Ta<sub>2</sub>N and Ta<sub>5</sub>N<sub>6</sub> phases were favored.<sup>12</sup> These observations, along with the depth profiling GIXS analysis, confirmed that N-poor phases are exclusively formed at the Ta<sub>3</sub>N<sub>5</sub>|Ta junction.<sup>5,12,13,19</sup> Domen *et al.*<sup>1</sup> showed that the ammonolysis of anodized Ta-substrate results in the formation of N-poor phases, e.g. Ta<sub>5</sub>N<sub>6</sub>, which limits the electron collection efficiency at the back contact. Interestingly, doping with barium suppressed the formation of the interfacial Ta<sub>5</sub>N<sub>6</sub> resistive layer, which substantially improved the PEC water oxidation performance of the electrode.

Importantly, these examples highlight the complexity of the synthesis of pure Ta<sub>3</sub>N<sub>5</sub> which requires a precise control over ammonolysis temperature, atmosphere, and reaction duration.<sup>20,21</sup> For example, Henderson and Hector<sup>20</sup> studied the structural and compositional evolution of Ta<sub>3</sub>N<sub>5</sub> from amorphous tantalum oxide as a function of ammonolysis temperature (from 680 to 900 °C) and duration (from 8h to 120h). Their results are quite remarkable, showing that regardless of

ammonolysis conditions (temperature or duration), all samples contained oxygen impurities - even after annealing at 900 °C for 120 h. In addition, Terao<sup>21</sup> showed that at elevated temperatures (>1000 °C) Ta<sub>3</sub>N<sub>5</sub> has a dynamic structure and composition where nitrogen is successively pulled out of the structure upon increasing temperature in vacuum – this is accompanied by the concomitant reduction of Ta<sup>V</sup> – which subsequently results in the formation of various phases of tantalum nitride. Therefore, it is highly beneficial to directly synthesize crystalline Ta<sub>3</sub>N<sub>5</sub> films at lower temperatures from oxygen-free precursors and atmosphere by eliminating the ammonolysis step. This approach is additionally beneficial as it allows integration of Ta<sub>3</sub>N<sub>5</sub> with different materials, e.g. with transparent conductive oxide (TCO) substrates for PEC investigations.

The vacuum deposition techniques such as atomic layer deposition (ALD) or chemical vapor deposition (CVD) provide an oxygen-free atmosphere suitable for the synthesis of non-oxide materials with a controllable thickness and composition. A series of previous studies for the deposition of tantalum nitride using ALD or CVD are listed in Table S1. Briefly, these studies indicate that tantalum halides, e.g. TaCl<sub>5</sub> and TaBr<sub>5</sub>, coupled with ammonia are commonly used the tantalum and nitrogen sources to directly deposit crystalline Ta<sub>3</sub>N<sub>5</sub> thin  $films.^{222324251826272829303132} \ The \ near \ atmospheric \ pressure \ CVD \ synthesis \ of \ Ta_3N_5 \ from \ these$ sources require a high deposition temperature of ≥ 900 °C, while the low-pressure CVD or ALD deposition can be done at considerably lower temperatures in the range of 400 – 500 °C. Inspired by these reports, we have endeavored to directly deposit crystalline Ta<sub>3</sub>N<sub>5</sub> films on FTO substrates *via* a custom-built and fully automated ALD system capable of operating at elevated temperatures with a maximum temperature of 640 °C. We showed that this technique provides a suitable method to integrate Ta<sub>3</sub>N<sub>5</sub> on relatively chemically unstable substrates like FTO in reducing atmospheres of ammonia. Success allowed the photoelectrochemical performance of Ta<sub>3</sub>N<sub>5</sub>|FTO electrodes with various thicknesses as a function of illumination direction to be explored, which elucidated the performance controlling processes of Ta<sub>3</sub>N<sub>5</sub> electrodes.

## **Experimental**

## Deposition of Ta<sub>3</sub>N<sub>5</sub> Film

The deposition of Ta<sub>3</sub>N<sub>5</sub> was carried out in a custom built ALD system described in detail in the supporting information. The films were deposited on F-doped tin oxide (FTO) coated glass

substrates (Tech 15, Hartford Glass Co) with the softening point of ~600 °C. The FTO-glass substrates were cut into hexagonal pieces with the diameter of ~ 5.2 cm. Prior to deposition, substrates were cleaned twice by sequential sonication in soap, water, and isopropyl alcohol for 15 minutes each (with the total time of 90 minutes). Prior to loading into the instrument, the FTO substrate was dried in a gentle flow of nitrogen. The Ta<sub>3</sub>N<sub>5</sub> films were deposited via sequential pulses of TaCl<sub>5</sub> (Alfa Aesar, 99.9%) as the source of tantalum and anhydrous ammonia (Airgas) as the co-reactant. The purified N<sub>2</sub> (99.9%) with the flow rate of 20 SCCM was used as the carrier gas. The TaCl<sub>5</sub> cylinder was kept at 120 °C and it was pulsed for 2 s which was followed by 15 s waiting/purging under the flow of nitrogen. Prior to pulsing ammonia, the nitrogen line is closed. This step is required to avoid contamination of carrier gas or TaCl<sub>5</sub> precursor. After a 5 s wait time, ammonia was pulsed for 0.1 s. This step is followed by a 10 s waiting time while the nitrogen line is closed and an additional 15 s purging time while the nitrogen line is in open position. The schematic representation of this recipe is shown in Figure S9. A range of substrate temperatures from 450 to 550 °C were investigated. The temperature of the substrate heater was externally calibrated with a secondary thermocouple (digital meter model 6802II equipped with a K-type thermocouple) and the calibration points can be found in Table S2. The measured temperature by both thermocouples are within  $\pm$  10 °C and throughout this manuscript we referred to the setpoint temperature. To study the stability of FTO under the deposition conditions of tantalum nitride we annealed the FTO glass substrate at 550 °C under a continuous flow of ammonia with a flow rate of  $\sim 100$  SCCM for 5 hours in a tube furnace equipped with a quartz tube (2.5"  $\times$  18"). We note that this annealing condition is far more extreme than the deposition conditions (as ammonia is continuously flowing and is not diluted with N<sub>2</sub>) thus it represents the upper limit for the stability of FTO.

#### Film Characterization

The morphology and thickness of the deposited films were examined using scanning electron microscopy (SEM, Carl Zeiss Auriga, Dual Column FIB-SEM). For the cross-section analysis, the films were coated with 5-10 nm tungsten conductive layer *via* sputtering (Denton Vacuum Desk II sputter coater). ImageJ software was utilized to analyze the thickness of the films from cross-section SEM.<sup>33</sup> The compositions of the deposited films were evaluated *via* energy dispersive spectroscopy (CARL ZEISS EVO LS 25) equipped with Ametek-EDAX Apollo X detector and

TEAD EDS software. The spectrum for each sample was normalized to its total area. The Raman spectra were collected *via* inVia Raman Microscope (Renishaw) equipped with 45 W cobalt DPSS laser (532 nm line) and a 100× microscope. Prior to Raman measurements, the instrument was quickly calibrated against an internal silicon standard. Raman spectra were normalized to the total area. The crystallinity and phase purity of the films were evaluated *via* X-ray diffraction (XRD) using Bruker D8 advanced diffractometer using Cu radiation at 1.5118 Å. It is important to note that during the XRD measurements the sample was spun to eliminate the artifact arising from the 2D structure of film by contributing all the plane and crystallites.

The optical properties of the Ta<sub>3</sub>N<sub>5</sub>|FTO films were determined with a PerkinElmer Lambda 35 UV-vis spectrometer equipped with Labsphere integrating sphere. The % absorptance (% A) was corrected for the substrate using a model previously described.<sup>34</sup> The Beer-Lambert law in combination with the absorption coefficient of Ta<sub>3</sub>N<sub>5</sub> at 450 nm (188,000 cm<sup>-1</sup>)<sup>35</sup> was utilized to calculate the film thickness. Photoluminescence (PL) spectra were measured using Hamamatsu Absolute PL quantum yield spectrometer C11347. Atomic force microscopy (AFM, Cypher Atomic Force Microscope/Scanning Probe Microscope (AFM/SPM)) in the tapping mode equipped with silicon AFM probe (Budget Sensor) with 300 kHz resonant frequency and 40 N/m force constant was utilized to measure the film roughness and topology. Reflectance mode spectroscopic ellipsometry (SE) measurements were acquired via Horiba Jobin Yvon, Smart-SE instrument, centered at Brewster angle of 70° over a photon energy range of 1.23 to 2.78 eV. Optical modeling were performed using DeltaPsi2 software (version 2.6). The SE measurement was performed on a Ta<sub>3</sub>N<sub>5</sub> (115 nm) film on a quartz substrate. The surface at the bottom of the quartz substrate was roughened with a coarse sandpaper to eliminate the backside light scattering and reflections. Hall measurements, using the van der Pauw method, were performed on Ta<sub>3</sub>N<sub>5</sub> layer having a thickness of ~115 nm as determined by cross-sectional SEM images. Indium contacts displaying ohmic characteristics were used to probe the samples. The measured electron concentration is  $2.31 \times 10^{19}$  ( $\pm 0.34$ ) cm<sup>-3</sup>, with an electron mobility of 0.19 ( $\pm 0.02$ ) cm<sup>2</sup>/V·s. The corresponding resistivity of the layer was measured to be 1.43 ( $\pm$  0.08)  $\Omega$ ·cm. X-ray photoelectron spectroscopy (XPS) was performed utilizing PerkinElmer Phi 5600 ESCA equipped with Mg Ka source where sample was illuminated at a takeoff angle of 45°. The binding energies (B.E.) were corrected by setting the C 1s peak at 284.8 eV.

#### **Photoelectrochemical Measurements**

The electrochemical measurements were carried out with an Autolab potentiostat (PGSTAT128N) equipped with Nova electrochemical software. A custom-built glass electrochemical cell equipped with a quartz window was used for all of the PEC measurement. The active surface area of the electrode is determined by the internal area of the O-ring (0.19 cm<sup>-2</sup>) that was used to clamp the electrode on the cell. The photoelectrochemical performance of the electrodes were carried out in contact with an aqueous solution containing 0.1 M K<sub>4</sub>[Fe(CN)<sub>6</sub>] as the hole scavenger with a pH of  $\sim$ 7. The current density (J) vs. potential (E) curves were measured at a scan rate of 20 mV/s. The photo-responses of the electrodes were measured as a function of illumination direction: the back illumination referring to illumination through the substrate and the front illumination referring to illumination through the solution. A 4500 W Xe lamp (Horiba Jobin Yvon) and AM 1.5 solar filter were used to simulate sunlight at the power of 100 mW cm<sup>-2</sup> (1 sun). The light intensity at the position of the electrode was calibrated with a certified reference cell (Oriel Reference Solar Cell & Meter). A homemade Ag/AgCl electrode which was calibrated against a commercial calomel electrode (Koslow Scientific), and a platinum mesh electrodes were utilized as the reference and counter electrode, respectively. The J-E performance of Ta<sub>3</sub>N<sub>5</sub> was also light (Autolab Blue LED, measured under monochromatic LED Catalog No. SNGEC0LELDC470) with the wavelength of 470 nm. The light intensity at the position of the electrode was determined with a Si photodiode (Thorlabs, FDS100-CAL). To accurately account for light attenuation due to electrolyte absorption, a quartz substrate (instead of working electrode) was mounted on the electrochemical cell. The cell was then filled with electrolyte and placed in front of Si photodiode. A low light intensity of 0.8 and 4.20 mW cm<sup>-2</sup> and a relatively higher scan rate of 50 mV/s was used to minimize the surface photocorrosion. The potential was scanned from -0.6 to 0.8 V vs. Ag/AgCl.

Electrochemical impedance spectroscopy (EIS) measurements were carried out at 10 mV amplitude perturbation in the 0.01 to 10,000 Hz frequency range. Under dark conditions, only one semicircle was observed in the Nyquist plot. The data were fit to the Randle circuit model using Zview software. The incident photon-to-current efficiency (IPCE) measurements were carried out in a three-electrode setup under monochromatic light in the 400 to 700 nm range with the 10 nm intervals. The white light was separated using a Horiba Jobin Yvon MicroHR monochromator with

600 line/mm. The entrance and the exit slits of the monochromator were set at 0.75 mm which corresponds to an 8 nm linewidth. The light intensity at the electrode position under monochromatic light was measured with Nova II Ophir. The IPCE and absorbed photon-to-current efficiency (APCE) values were calculated according to Equation 1 and Equation 2, respectively, where  $\lambda$  is the wavelength of excitation, and  $J_{ph}$ ,  $P_{mono}$ , and %A are the photocurrent density, power density, and absorbtance of the film respectively measured at wavelength  $\lambda$ .

IPCE(%) = 
$$100 \times \frac{J_{\text{ph}}(\text{mA cm}^{-2}) \times 1239.8 \text{ (V nm)}}{P_{\text{mono}}(\text{mW cm}^{-2}) \times \lambda \text{ (nm)}}$$
 Equation 1

$$APCE(\%) = 100 \times \frac{\% \text{ IPCE}}{\% \text{ A}}$$
 Equation 2

#### **Results and Discussion**

A range of substrate temperatures from 450 to 550 °C was investigated for the deposition of  $Ta_3N_5$  on FTO using  $TaCl_5$  as the Ta-source and  $NH_3$  as the N-source. From the results of XRD measurements, it was found that 550 °C is the minimum temperature required to deposit crystalline  $Ta_3N_5$  on the FTO substrates used here. In agreement with our previous observations,  $^{18}$  we find that at the temperatures beyond 550 °C the FTO substrate is not stable under ammonia/ vacuum conditions (a highly reducing atmosphere) and it becomes flaky and loses its inherent properties of conductivity and transparency as a TCO. We note that this temperature is higher by 50 - 150 °C in comparison to the previous studies on ALD deposition of  $Ta_3N_5$  (summarized in Table S1).  $^{24,25}$  The higher temperature required to deposit crystalline films found here may be due to the difference in the ALD reactor configuration and substrate used.

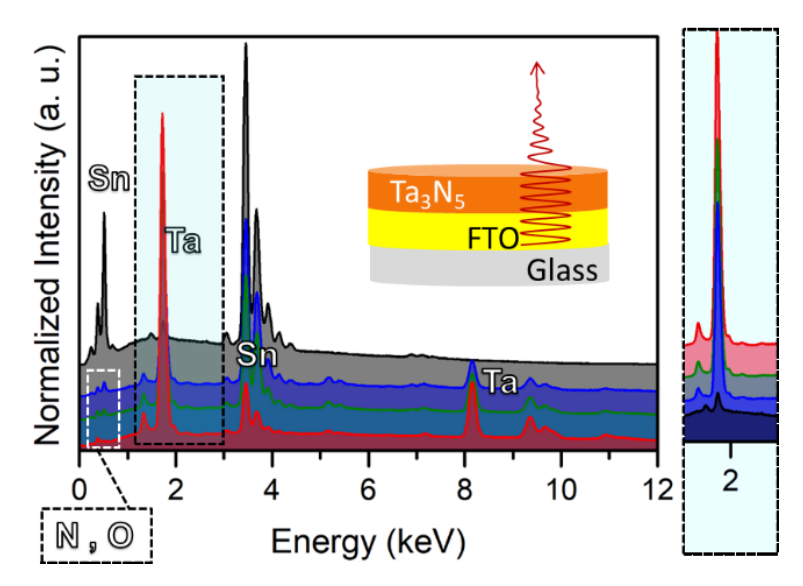


**Figure 2.** The EDS spectra of the bare FTO (black) and the deposited films as a function of the number of cycles; 150 cycles (blue), 300 (green) and 500 (red). The highlighted graph on the right-hand side represents the peak located at 1.7 keV in a reverse order showing a progressive growth of Ta peak as the number of cycles increases. The inset represents the configuration of the film and the origin of signals.

Energy dispersive spectroscopy (EDS) was utilized to assess the composition of the deposited films. The EDS spectra for the bare FTO and the as-deposited films as a function of the number of cycles are compared in Figure 2. Due to the large sampling depth of this technique, in addition to the deposited film (top layer), the FTO substrate (SnO<sub>2</sub>) is detected. The observed peaks are then assigned to Ta, Sn, O, and N (the list of characteristic X-rays for these elements is summarized in Table S3). The broad peaks located at 0.69 and 3.4 keV are attributed to tin (Sn) from the FTO substrate. For a similar beam energy (15 kV), this peak has the highest intensity for the bare FTO substrate but its intensity progressively declines as the number of deposition cycles increases. Concomitantly, the intensity of Ta peaks (at  $\sim 1.7$  and 7 > keV) grows with the number of cycles used. This is an important observation as it readily indicates that the deposited material forms a layer on top of the FTO substrate and that its thickness grows with the number of cycles. While these spectra confirm the presence of nitrogen (peak at ~ 0.4 keV), due to the low sensitivity of this technique to the light elements the ratio of Ta to N cannot be determined accurately. We also note that for all thicknesses no signature of chloride as an impurity was observed. This observation is further supported by the XPS analysis of Ta<sub>3</sub>N<sub>5</sub> films with different thickness where Ta, N, and O were the primary signals observed (Figure S10 and Figure S11). Altogether, these observations indicate that the reaction between ammonia and tantalum chloride runs to completion. Based on

both survey and detailed XPS measurements, no signal for Sn was observed (except for the film with 150 cycles, discussed following Figure S11). Importantly, this observation implies that the ALD deposition conditions used here is mild and excludes the diffusion and doping of Sn, yielding pristine Ta<sub>3</sub>N<sub>5</sub> films.

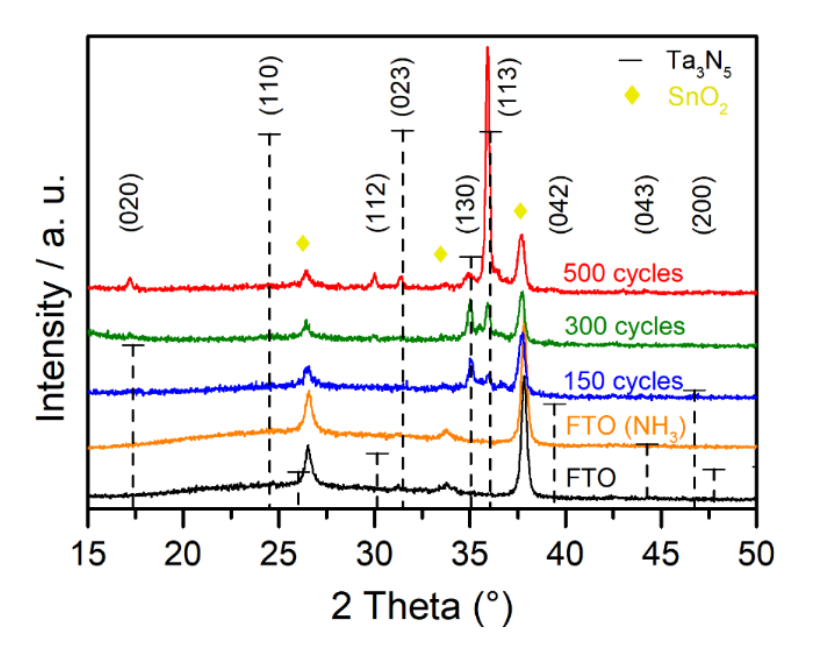


**Figure 3**. The XRD patterns of the FTO  $(SnO_2)$  substrates before (black) and after (orange) annealing in ammonia and tantalum nitride films with various thicknesses on FTO substrate. Films with 150 cycles, 300, and 500 cycles are shown in blue, green, and red colors, respectively. The vertical black dashed lines represent the Bragg positions for the standard crystalline  $Ta_3N_5$  powder with random crystal orientations (PDF # 01-079-1533). The numbers represent the Miller indices of the corresponding diffraction peaks of  $Ta_3N_5$ . The yellow diamonds represent the Bragg positions of the standard  $SnO_2$  (PDF # 00-046-1088).

The XRD diffraction patterns of the bare FTO substrates before and after annealing in ammonia with a flow rate of 100 SCCM at 550 °C for 2 h are compared to the deposited films with various numbers of cycles in Figure 3. The diffraction patterns for the bare FTO substrates before and after ammonolysis (control samples) are identical and are assigned to SnO<sub>2</sub>. The measured diffraction patterns for the deposited films (for all thicknesses) are unambiguously assigned to Ta<sub>3</sub>N<sub>5</sub> and SnO<sub>2</sub>. In addition, the peak positions of SnO<sub>2</sub> for the deposited films are identical to that of the control samples. These observations collectively indicate that FTO is structurally stable under the deposition conditions of the crystalline Ta<sub>3</sub>N<sub>5</sub>. Interestingly, we note that under identical XRD measurement conditions, the ratio of the diffraction intensities of SnO<sub>2</sub> to Ta<sub>3</sub>N<sub>5</sub> progressively

decreases with increasing Ta<sub>3</sub>N<sub>5</sub> thicknesses. In agreement with the EDS data shown in Figure 2, this observation indicates that the deposited films form a layer over the FTO substrates.

A closer inspection of the XRD pattern as a function of film thickness reveals a strong correlation between the pattern of diffraction (relative peak intensities) and the number of deposition cycles. In comparison to the diffraction pattern of the randomly oriented reference Ta<sub>3</sub>N<sub>5</sub> (vertical dashed lines), it can be realized that the diffraction peak located at 24.6° (Miller indices of (110)) - which is one of the most intense diffractions for the reference - is missing for all of the films. For this to occur, the (110) plane must be perpendicular to the substrate, implying that the deposited films exhibit a preferential orientation. A detailed analysis of the crystal orientation of the films is discussed following Figure S12. In addition, the relative intensity of the (130) plane to the (113) plane strongly depends on the number of deposition cycles; it approaches the relative ratio observed for the randomly oriented reference pattern as the number of cycles increases. It can therefore be hypothesized that the different lattice structure of Ta<sub>3</sub>N<sub>5</sub> compared to SnO<sub>2</sub> results in a lattice mismatch, such that the initial growth mode of Ta<sub>3</sub>N<sub>5</sub> is different and proceeds through the formation of a buffer layer on the FTO substrate. Following the formation of the buffer layer, as the number of cycles increases, the effect of the lattice mismatch on the rest of the bulk film is minimized and  $Ta_3N_5$  grows approximately randomly. Therefore, the growth rate and morphology of the crystalline Ta3N5 formed by this method are expected to be strongly substrate-dependent.

To further investigate this point a film with 300 cycles of  $Ta_3N_5$  was deposited on a quartz substrate. The crystallinity, morphology, and thickness of the film were investigated via XRD and SEM. Based on the cross-section SEM, 300 cycles deposition results in a  $Ta_3N_5$  film with  $\sim 115$  nm thickness (Figure S13.a) which is somewhat close to the thickness of the film found on FTO substrate (discussed below). Interestingly, the top morphology of the  $Ta_3N_5$  films with approximately similar thicknesses varies between quartz and FTO substrate (Figure S13b and Figure 4). In addition, as shown in Figure S14, the X-ray diffraction pattern (the relative intensity of the peaks) of  $Ta_3N_5$  films on quartz is drastically different than the  $Ta_3N_5$  films on FTO with relatively the similar thicknesses (115 vs. 103 nm). Altogether, these data strongly indicate that the growth mode of crystalline  $Ta_3N_5$  (i.e. rate, crystal orientations, and morphology) depends on the substrate.

The Raman spectra of films with different thicknesses are compared in Figure S15. In line with the XRD measurements, the observed phonon modes are consistent with crystalline  $Ta_3N_5$ . The SEM images of the bare FTO substrates before and after annealing in ammonia are shown in Figure S16. As depicted, while after annealing in ammonia some surface aggregations are observed, the film thicknesses are a constant  $\sim 240$  nm. In line with the XRD patterns of the FTO (Figure 3), this observation further indicates that the  $SnO_2$  phase is stable under the reducing atmosphere of ammonia. The top view and cross-section SEM, as well as the AFM images of  $Ta_3N_5$  films of various thicknesses, are compared to the bare FTO substrate in Figure 4. The cross-section SEM images clearly show that the films are comprised of two distinct layers of  $Ta_3N_5$  (top layer) and FTO (bottom layer). The  $Ta_3N_5$  films are compact, and their thicknesses increase with the number of cycles, whereas the thickness of the FTO layer remains constant. Due to the lack of a visually sharp interface between these two layers, the thickness of the  $Ta_3N_5$  film was calculated by subtracting the original thickness of the FTO layer (240 nm) from the total thickness.

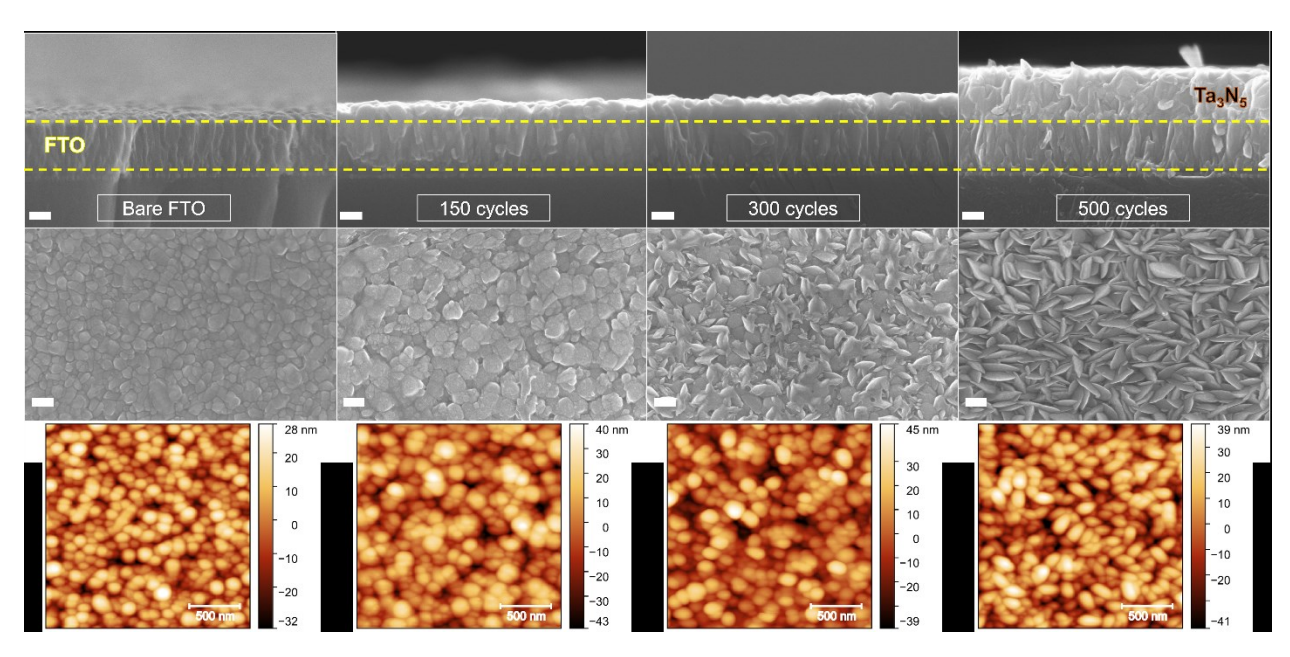


**Figure 4.** The SEM and AFM images showing the cross-section, morphology, and topography of the bare FTO and  $Ta_3N_5$  films of different thicknesses. The scale bars for the SEM images are 200 nm with  $\sim 200,000X$  magnification. The 3D AFM images are shown in Figure S17.

The thicknesses of the films with 150, 300, and 500 cycles was found to be 70, 103, and 230 nm, respectively. Based on the top view SEM and AFM topography images, the morphologies of the films is strongly correlated to the number of cycles (film thickness). The film with 70 nm thickness

has a similar spherical morphology to the FTO substrate but with bigger features and a porous morphology. Interestingly, the morphology of the film with 103 nm thickness begins to deviate from the FTO substrate exhibiting new oval-shape features where the film with 230 nm thickness only exhibit a randomly distributed oval-shape features perpendicular to the surface. AFM was used to assess the surface roughness as a function of ALD cycles (summarized in Table S4). Consistent with SEM results, it was noted that the mean RMS roughness of  $Ta_3N_5$  films with 70 and 103 nm are similar to the bare FTO substrate,  $\sim 15$  nm. However, an increase of 5 nm in RMS roughness was observed for the film with 230 nm thickness. The morphology and surface roughness evolutions as a function of the film thickness described here follow the same trend as the evolution of the XRD pattern which similarly can be ascribed to the difference in the crystal structure of  $Ta_3N_5$  and FTO as described above.

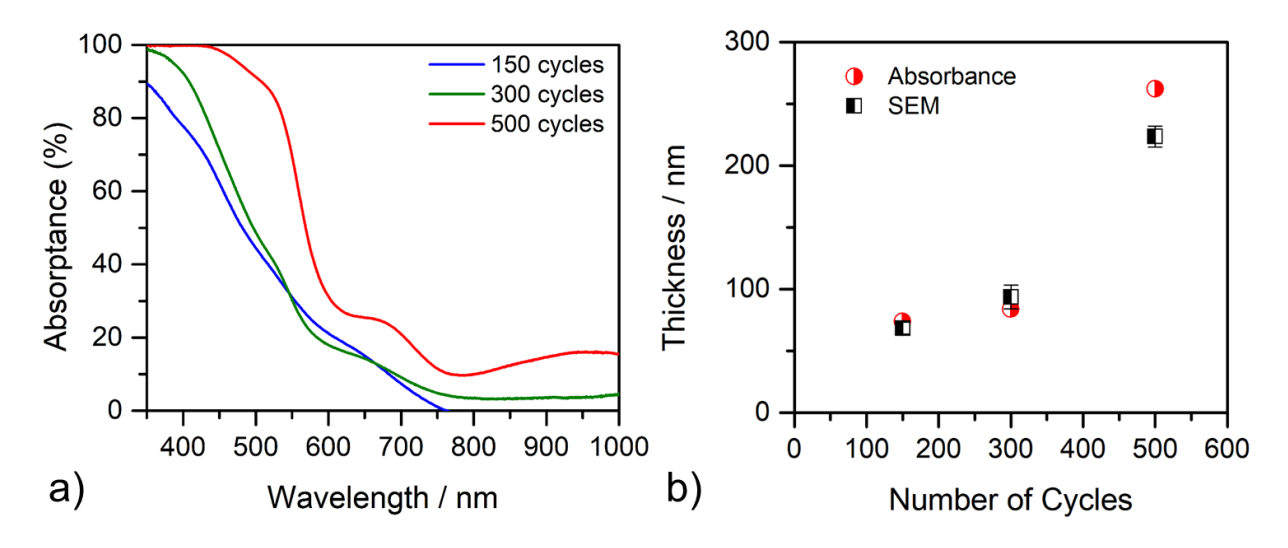


**Figure 5.** a) Plots of the absorptance of  $Ta_3N_5$  films on FTO substrate with various thicknesses. The corresponding transmittances and reflectances are shown in Figure S19. The data shown here are corrected for the FTO substrate using the previously reported procedure.<sup>34</sup> b) The thickness of deposited films as a function of the number of cycles grown at 550 °C on FTO substrate. The thickness of the these films was determined *via* two independent methods of cross-section SEM analysis (black square) and the optical absorbance at 450 nm (red circle) in combination with beer-lambert law using the known absorption coefficient reported previously for a compact film of  $Ta_3N_5$ .<sup>35</sup>

The optical properties of bare FTO substrates before and after annealing in ammonia are shown in Figure S18. While the reflectance of the FTO substrate is not affected by the annealing in ammonia, the transmittance is reduced by  $\sim 10\%$ . This reduction can be ascribed to the surface agglomeration

observed in the SEM image (Figure S16). The absorptance spectra for various thicknesses of Ta<sub>3</sub>N<sub>5</sub> on FTO substrates are shown in Figure 5a. The absorptance edge for these films occurs at 575 -600 nm which is in good agreement with the known 2.1 eV bandgap of Ta<sub>3</sub>N<sub>5</sub>. <sup>18,36,37</sup> Clearly, the absorptance beyond the bandgap edge does not reach zero and it is more pronounced for thicker films. In addition, a well-resolved sub-bandgap absorption peak centered at ~ 700 nm is uniquely observed for the film with 300 and 500 cycles. It is important to note that the non-zero sub-band gap absorption is not specific to the ALD deposited Ta<sub>3</sub>N<sub>5</sub> films and indeed is observed for Ta<sub>3</sub>N<sub>5</sub> synthesized with various methods. 2,5,38-40 The origin of this absorption feature has been assigned to two completely distinctive sites: (1) the reduced Ta<sup>5+</sup> sites, i.e. Ta<sup>4+</sup> or Ta<sup>3+</sup>, <sup>39,40</sup> and (2) Nvacancy as a deep donor accompanied by a free electron in the conduction band to compensate the positive charge of the anion vacancy.<sup>5,38</sup> The main difference between these two sites is that the first one can serve as a trap state where the charges are localized on the Ta-sites while in the second one the charge is delocalized in the conduction band. The Hall measurements revealed a high dopant density ( $10^{19}$  ( $\pm 0.34$ ) cm<sup>-3</sup>) and a low electrical resistivity (1.43 ( $\pm 0.08$ )  $\Omega \cdot$  cm) for these films. The high dopant density further indicates that the sub-band gap absorption originates from the N-vacancy defects. Interestingly, non-zero sub band gap absorption is also observed the for the-state-of-the-art Ta<sub>3</sub>N<sub>5</sub> with porous cubic morphology by Li and coworkers.<sup>2</sup> Moreover, Jaramillo and coworkes<sup>12</sup> concluded that a high density of defects improves the charge mobility and are beneficial to realize high performing Ta<sub>3</sub>N<sub>5</sub> photoelectrode. Collectively, these observations indicate that the presence of these defects are not detrimental to the PEC performance of Ta<sub>3</sub>N<sub>5</sub>.

Previously, it was shown that Ta<sub>3</sub>N<sub>5</sub> films prepared by ammonolysis of Ta<sub>2</sub>O<sub>5</sub> exhibited a PL peak at 561 nm which was ascribed to a deep-level defect recombination of oxygen contaminated (doped) Ta<sub>3</sub>N<sub>5</sub> phase.<sup>41</sup> We note that the room temperature PL spectrum for different thicknesses of Ta<sub>3</sub>N<sub>5</sub> prepared in this study are noisy and featureless (Figure S20). The lack of a clear PL peak suggests that oxygen contamination is minimized for these ALD prepared Ta<sub>3</sub>N<sub>5</sub> films and that vacuum deposition techniques, e.g. ALD or CVD, are promising approaches to prepare pristine non-oxide semiconductors.

Figure 5a also shows that the absorptance of all the films do not scale with the number of cycles as expected; the film with 300 cycles has only a slightly higher absorptance than the film with 150

cycles. The plot of thickness vs. number of cycles acquired by the cross-section SEM and absorbances are shown in Figure 5b. We note that the film thicknesses found by these methods are different by as much as ~ 50 nm for the thickest film which can be ascribed to the uncertainty in the absorption coefficient and/or the calculated absorbance or change in the density of the films with various thicknesses. The trend in the film thickness as a function of the number of cycles between two methods are remarkably similar, however. As shown, within the window of the number of cycles studied here, the growth of tantalum nitride on FTO substrate is not linear. This phenomenon can be better understood by considering the growth of the crystalline tantalum nitride on FTO films. Consistent with the XRD and SEM images, the trend of the film growth indicates that the deposition of the tantalum nitride initiates by seeding and formation of a buffer layer for the first 150 cycles. Based on these thicknesses, the apparent growth rate of the Ta<sub>3</sub>N<sub>5</sub> films on FTO is  $\sim 0.46$  nm per cycle. We note that this growth rate is substantially higher than the previously reported values for the ALD deposition of crystalline tantalum nitride by a factor of ~ 18 (see Table S1). For example, Ritala et al. 24 utilized TaCl<sub>5</sub> and NH<sub>3</sub> to deposit Ta<sub>3</sub>N<sub>5</sub> on soda lime glass and ITO glass substrates. Under ALD growth conditions, i.e. self-terminating surface reaction, they reported an average growth rate of 0.025 nm per cycle at the temperature range of 400 to 500 °C. It is also worth noting that a growth rate of 0.46 nm per cycle is larger than the average bond length of Ta-N (0.21 nm) in Ta<sub>3</sub>N<sub>5</sub> by a factor of  $\sim 2.2.^{42}$  These observations collectively indicate that the deposition of Ta<sub>3</sub>N<sub>5</sub> reported here is not under self-limiting ALD deposition conditions. However, the higher growth rate of the film with a controlled thickness found here is advantageous as it minimizes the processing time to prepare tantalum nitride films.

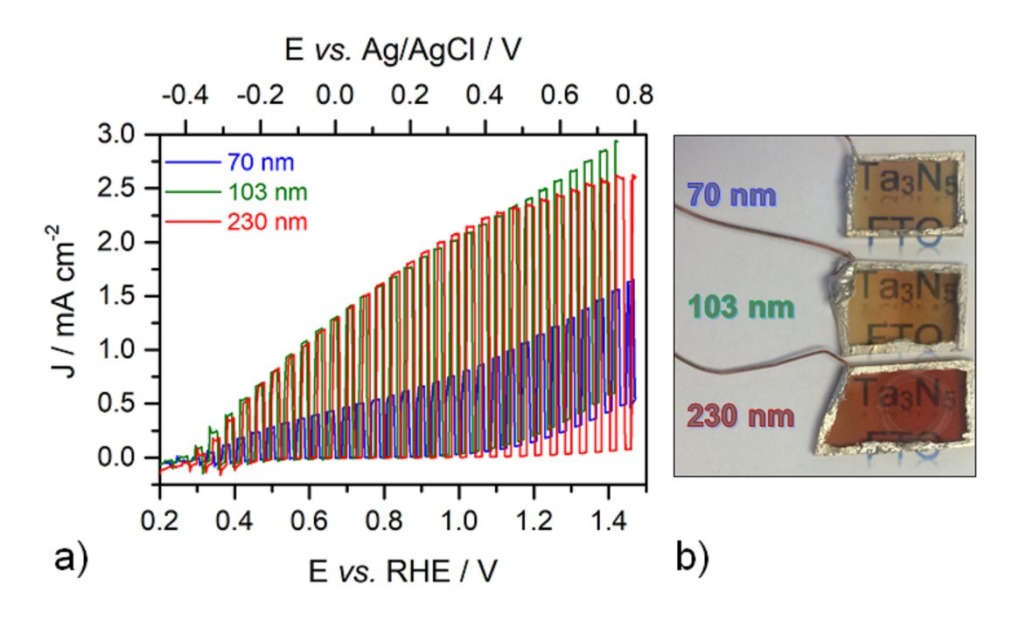


**Figure 6.** a) The chopped light *J-E* curves of Ta<sub>3</sub>N<sub>5</sub> on FTO substrate as a function of film thickness in contact with an aqueous solution containing 0.1 M K<sub>4</sub>[Fe(CN)<sub>6</sub>] as the hole scavenger with the pH of 7. The potential was scanned at 20 mV s<sup>-1</sup> and the electrodes were illuminated through the electrolyte with 1 sun intensity. b) The photograph of the electrodes with various thicknesses of Ta<sub>3</sub>N<sub>5</sub> on FTO substrate. As shown all the edges of the rectangular shape electrode were coated with Ag epoxy and the electrode was clamped to a custom made electrochemical cell with an O-ring with the diameter of 0.19 cm<sup>-2</sup> (the mark of the O-ring is partially visible on the 500 cycles electrode).

The *J-E* curves in presence of the one-electron fast hole scavenger along with the photograph of the electrodes with various thicknesses are shown in Figure 6. A prior example of  $Ta_3N_5$  on FTO substrates was reported by Higashi *et al.*<sup>43</sup>. They used the electrophoretic deposition to prepare mesoporous films from nanoparticle  $Ta_3N_5$ . The best performance was achieved by treating the asprepared films with  $TaCl_5$  followed by ammonolysis at 500 °C. The other example of  $Ta_3N_5$  photoanode on a transparent conductive substrate was reported by our group prepared *via* ALD of tantalum oxynitrides on Ta-doped  $TiO_2$  followed by ammonolysis. <sup>18</sup> To the best of our knowledge, this is the first example of directly deposited crystalline  $Ta_3N_5$  photoanode on a transparent conductive substrate. The *J-E* curves reported here produce a photocurrent onset potential of  $\sim 0.3$  V vs. RHE. This potential is comparable to the onset potential reported by Jaramillo *et al.* for the tandem core-shell Si- $Ta_3N_5$  photoanode and also the high performing nanostructured  $Ta_3N_5$  photoanodes introduced by Wang and coworkers. <sup>3,4,44</sup> The early photocurrent onset potential readily implies that FTO is sufficiently conductive that the energy lost for electron collection and transport is minimized. This observation is further supported by the conductivity measurement of

the FTO substrate before and after annealing in ammonia. As shown in Figure S21 the slopes of the J-E curves for both electrodes are nearly identical confirming that FTO is stable and remains conductive under the reducing conditions of ammonia at 550 °C. Another feature of the chopped light J-E curves shown in Figure 6 is the saturation of photocurrent density for the film with 103 nm thickness. The current saturation indicates that the transport of the holes (minority charge carrier) is limiting while electrons are efficiently collected at 230 nm thickness. The latter can be ascribed to the high dopant density found for Ta<sub>3</sub>N<sub>5</sub> (discussed below).

The chopped light J-E curves for Ta<sub>3</sub>N<sub>5</sub> films with various thicknesses as the function of illumination direction (front vs. back) are compared in Figure S22. We note that while the photocurrent onset potential is independent to the illumination direction, the photocurrent density strongly correlates to the illumination direction, however. In addition, unlike front illumination, the back illumination photocurrent versus film thickness initially grows by increasing the thickness from 70 nm to 103 nm, then it declines to lower values for the film with 230 nm film, following a peak shape profile. The 70 nm film produces a relatively constant photocurrent regardless of the illumination direction. However, as the film thickness grows the photocurrent density for the front and back illumination start to diverge with the front illumination constantly producing higher a photocurrent density with a maximum value of ~ 2.4 mA cm<sup>-2</sup> at 1.23 V vs. RHE. While this value falls short of the theoretical photocurrent (~ 12.5 mA cm<sup>-2</sup>) and the best examples of Ta<sub>3</sub>N<sub>5</sub> photoelectrode<sup>1-4</sup>, though, it is important to note that these high performing electrodes are high aspect ratio with nanostructured morphologies whereas the ALD deposited electrodes in this study are compact planner films (Figure 4). Jaramillo and coworkers<sup>45</sup> have recently shown that the photocurrent density of Ta<sub>3</sub>N<sub>5</sub> predominantly depends on the effective surface area of electrode. Altogether, we tentatively ascribed this relatively low photocurrent to the limited hole transport characteristics of Ta<sub>3</sub>N<sub>5</sub> and the planner morphology of these ALD deposited electrodes. The PEC performance of Ta<sub>3</sub>N<sub>5</sub> under water oxidation conditions was also assessed by linear sweep voltammetry under chapped light illumination (Figure S23). In comparison with ferrocyanide hole scavenger, under water oxidation condition, the planner Ta<sub>3</sub>N<sub>5</sub> photoelectrode produced lower photocurrent density (~ 0.4 mA cm<sup>-2</sup> at 1.23 V vs. RHE) with the photocurrent onset potential shifted anodically to  $\sim 0.8 \text{ V}$  vs. RHE. Successive J-E measurements showed a fast decay in the PEC performance of Ta<sub>3</sub>N<sub>5</sub> photoelectrode. These observations are consistent with the fast surface photocorrosion of Ta<sub>3</sub>N<sub>5</sub> and its low surface catalytic activity toward water oxidation.

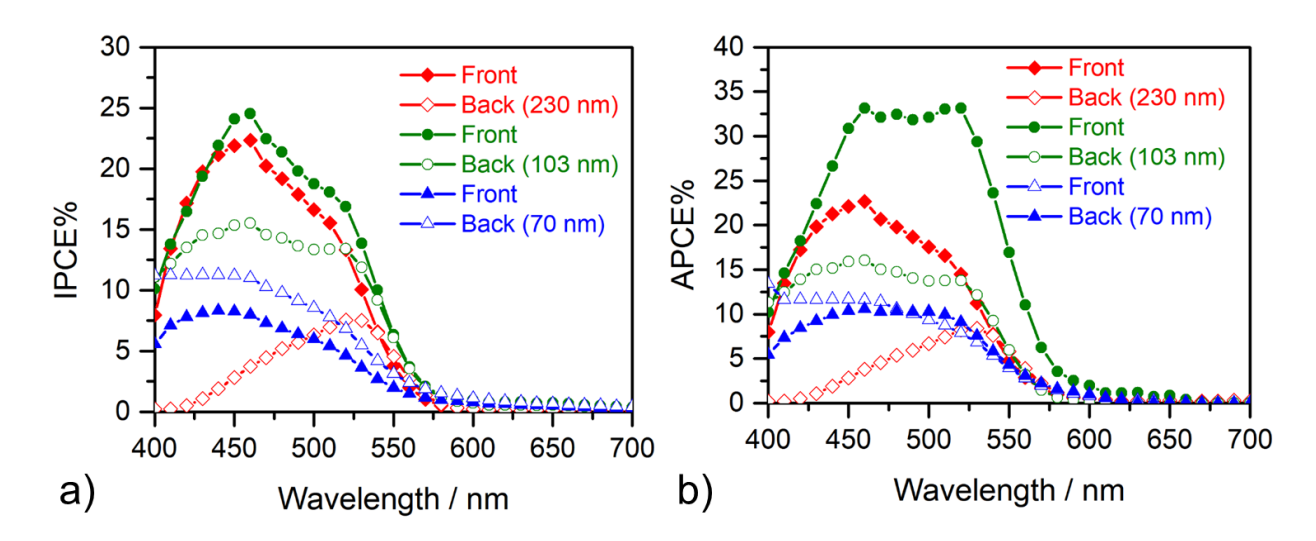


**Figure 7.** Wavelength dependence of the a) IPCE% and b) APCE% values at 1.0 V vs. RHE for the  $Ta_3N_5$  films with different thicknesses as a function of illumination direction in contact with an aqueous solution containing 0.1 M  $K_4[Fe(CN)_6]$  as the hole scavenger with the pH of 7. The solid and open shapes represent the values under front (through the solution) and back (through the substrate) illumination, respectively.  $Ta_3N_5$  films with 230, 103, and 70 nm thicknesses are shown in red diamond, green circle, and blue triangle, respectively.

Figure 7a shows the wavelength dependence of IPCE for various thicknesses of Ta<sub>3</sub>N<sub>5</sub> as a function of illumination direction. The onset of IPCEs for all the thicknesses of these electrodes is located around 575 nm which is in good agreement with the known 2.1 eV band gap for Ta<sub>3</sub>N<sub>5</sub>, <sup>18,36,37</sup> indicating that the observed photoresponse is due to the Ta<sub>3</sub>N<sub>5</sub> film. The sharp decline in the IPCE values observed in the front illumination (through electrolyte) at the wavelengths below 450 nm can be ascribed to the absorption of the ferri/ferrocyanide solution. <sup>46</sup> In agreement with the *J-E* curves shown in Figure S22, the front IPCE is larger than the back IPCE, which indicates that the transport of holes is kinetically limiting. The back IPCE response initially increases as the film thickness grows but steeply declines for the 230 nm thick film. In addition, the back IPCE values for the films with 70 and 103 nm thicknesses plateau with average values of approximately 10 and 15%, respectively. Conversely, the back IPCE% for the 230 nm Ta<sub>3</sub>N<sub>5</sub> electrode produced a peak at 525 nm and declined to zero for the lower wavelengths.

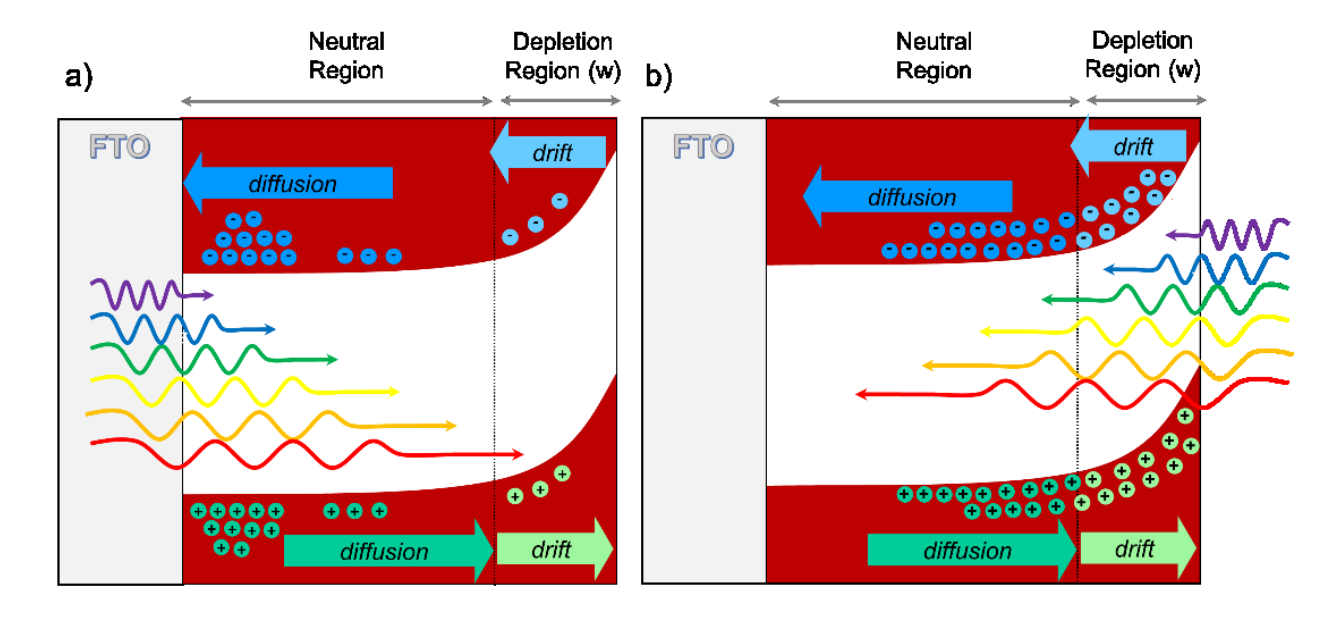


**Figure 8.** The schematic representation of the profile of charge generation as a function of illumination direction; a) back illumination (through the FTO), b) front illumination (through the solutions).

These observations can be better understood by considering the absorption penetration depth of tantalum nitride and the profile of photogeneration of charge carriers as a function of illumination direction (shown in Figure 8). The penetration depth of light for  $Ta_3N_5$  for the photons with the wavelength of 525 and 450 nm are 120 and 52 nm, respectively. As a result, the back illumination photons with larger penetration depths (red photons) produce charge carriers within the diffusion length of the holes to the surface while the short wavelength light (blue photons) with short absorption lengths predominately generate holes close to the FTO substrate. As the result, for the film with 230 nm thickness, the back IPCE produces a peak rather than a constant value. The APCE values of these films as a function of illumination direction for various thicknesses are shown in Figure 7b. The maximum APCE is observed for the film with 103 nm thickness. For 230 nm thick  $Ta_3N_5$  films, even though the absorptance is quantitative (Figure 5a), the APCE decreases which indicates that for this films the charge carriers are produced outside of the holes diffusion length and thus do not contributed to the photocurrent.

EIS measurements were used to assess the electrical properties of  $Ta_3N_5$  films on FTO substrates. The EIS responses were fit to the Randle circuit to extract the capacitance of the space charged region ( $C_{\text{bulk}}$ ). The Mott-Schottky (MS) plot of  $Ta_3N_5$  with 103 nm thickness in dark is shown in

Figure S24. The dopant density ( $N_d$ ) was calculated by fitting the linear region to the MS equation (Equation 3)<sup>47</sup>:

$$\left(\frac{A}{C_{\text{bulk}}}\right)^2 = \left(\frac{2}{q\varepsilon\varepsilon_0 N_{\text{d}}}\right) \left(V_{\text{app}} + V_{\text{FB}} - \frac{k_B T}{q}\right)$$
 Equation 3

In this equation, A,  $k_B$ , T, q,  $\varepsilon$ ,  $\varepsilon_0$ , and  $V_{app}$  are the geometrical surface area, Boltzmann's constant, absolute temperature, elementary charge, the dielectric constant of semiconductor, permittivity of free space, and applied voltage, respectively. We note that in the literature there is no agreement on the dielectric constant of Ta<sub>3</sub>N<sub>5</sub> and different values ranging from 7 to 110 have been reported (Table S5). <sup>1,35,36,48,49</sup> This wide range of dielectric constant can be ascribed to variations in crystallinity and composition (presence of oxygen impurity and vacancies) of Ta<sub>3</sub>N<sub>5</sub>. For consistency of our analysis, thus, we utilized SE to assess the dielectric constant for Ta<sub>3</sub>N<sub>5</sub> films prepared in this study. The detailed description of SE modeling and results are discussed following Figure S25 and Table S5. Using a previously developed procedure for modeling the optical properties of Ta<sub>3</sub>N<sub>5</sub>, <sup>36</sup> a dielectric constant of 21.6 ( $\pm$  1.2) was calculated. This value is in close agreement with a dielectric constant of 17 (calculated optically). <sup>35</sup>

From linear fit of data to MS equation (Equation 3) and using a dielectric constant of 21.6, a dopant density of  $3.26 \times 10^{20}$  cm<sup>-3</sup> was calculated (the dopant density for different values of dielectric constant are summarized in Table S6). To independently evaluate the dopant density of  $Ta_3N_5$ , the Hall-effect measurement was utilized, and a dopant density of  $2.31 \times 10^{19}$  ( $\pm 0.34$ ) cm<sup>-3</sup> was calculated. We note that this value is about 14 times smaller than the number calculated from EIS method. This difference can be ascribed to the uncertainty in the actual surface area of the electrode that was used for EIS calculations. Flat band potential was calculated from the intercept of the linear fit to Equation 3, as 0.19 V vs. RHE. The solution potential of  $[\text{Fe}(\text{CN})_6]^{3./4-}$  is 0.68 V vs. RHE (measured in two-electrode system), and the built-in voltage ( $V_{bi}$ ) is  $\approx 0.49 \text{ V}$ . The depletion width (w) was calculated according to Equation 4. The calculated depletion width based on the dopant density from EIS and Hall measurements are 1.9 and 6.87 nm, respectively. As summarized in Table S6, the depletion width for various dielectric constants found in literature all lie below 10 nm. This narrow depletion width can be ascribed to the high dopant density.

$$w = \sqrt{\frac{2\varepsilon\varepsilon_0 V_{\text{bi}}}{\text{qN}_{\text{d}}}}$$
 Equation 4

Due to the narrow depletion width and the large absorption depth of Ta<sub>3</sub>N<sub>5</sub>, a significantly small number of charge carriers are generated in the depletion region which cannot account for the observed photocurrent densities. Since the depletion width is narrow in comparison to the thinnest film here (70 nm), thus the PEC performance of Ta<sub>3</sub>N<sub>5</sub> is controlled by the diffusion of photogenerated holes.

To calculate the hole diffusion length (minority charge carriers) in Ta<sub>3</sub>N<sub>5</sub>, the Gärtner model and corrected-Gärtner model (Equation 5) were utilized: <sup>50–52</sup>

$$\frac{J(V)_{\text{photo}}}{J_0} = \left\{ \left( 1 - \frac{e^{-\alpha W(V)_{SC}}}{1 + \alpha L_p} \right) \left( \frac{1 - R}{100} \right) \right\} \text{TE(V)}$$
 Equation 5

where *J*<sub>photo</sub>, *J*<sub>0</sub>, α, *L*<sub>p</sub>, R, and TE are photocurrent response, theoretical current density, absorption coefficient, diffusion length of holes, reflectance, and surface hole collection efficiency, respectively. The Gärtner model (shown in curly bracket on the right-hand side of Equation 5) assumes that the reaction of holes at the surface of electrode is fast and the hole collection at the surface of electrode is quantitative. In addition, it is assumed that electron-hole recombination at the surface of electrode and depletion region is negligible.<sup>50,51</sup> Clearly, these conditions are only valid for ideal semiconductor and semiconductor|electrolyte junctions. To accurately account for surface recombination and slow hole transfer at the surface of electrode, an additional term, "surface hole collection efficiency", was added to the Gärtner model. Wang and coworkers<sup>52</sup> successfully applied this correction to simulate the photocurrent–potential performance of hematite electrodes. In this study, we used transient current measurements<sup>53–56</sup> to determine TE at various potentials. The detailed description of calculations are discussed in supporting information following Figure S26.

The normalized experimental and simulated J-E curves of Ta<sub>3</sub>N<sub>5</sub> under monochromatic blue light (470 nm) are shown in Figure 9. As shown, the corrected-Gärtner model using the experimentally

determined TE at various potentials (Figure S24) results in a hole diffusion length of 50 nm. Evidently, the simulated curve using corrected-Gärtner model closely reproduces the experimental results and closely predicts the *J-E* curve. On the other hand, while the simulated curve based on the Gärtner model for a hole diffusion length of 50 nm accurately predicts the photocurrent onset potential, however, the simulated *J-E* curve is drastically different than the experimental results. The difference in simulated curves using Gärtner model and corrected-Gärtner model readily indicates that the surface electron-hole recombination is a serious issue for Ta<sub>3</sub>N<sub>5</sub>|aqueous electrolyte junction. Clearly, even in presence of a fast hole scavenger, surface recombination substantially suppresses the performance of Ta<sub>3</sub>N<sub>5</sub>. This observation is further in agreement with a recent study by Wang and coworkers<sup>3</sup> on the surface corrosion of Ta<sub>3</sub>N<sub>5</sub>. They showed that in aqueous electrolyte, even in presence of fast hole scavengers, and under PEC conditions the surface of Ta<sub>3</sub>N<sub>5</sub> is readily oxidized, forming an insulating layer of tantalum oxide on the surface which pins the Fermi level of Ta<sub>3</sub>N<sub>5</sub>.

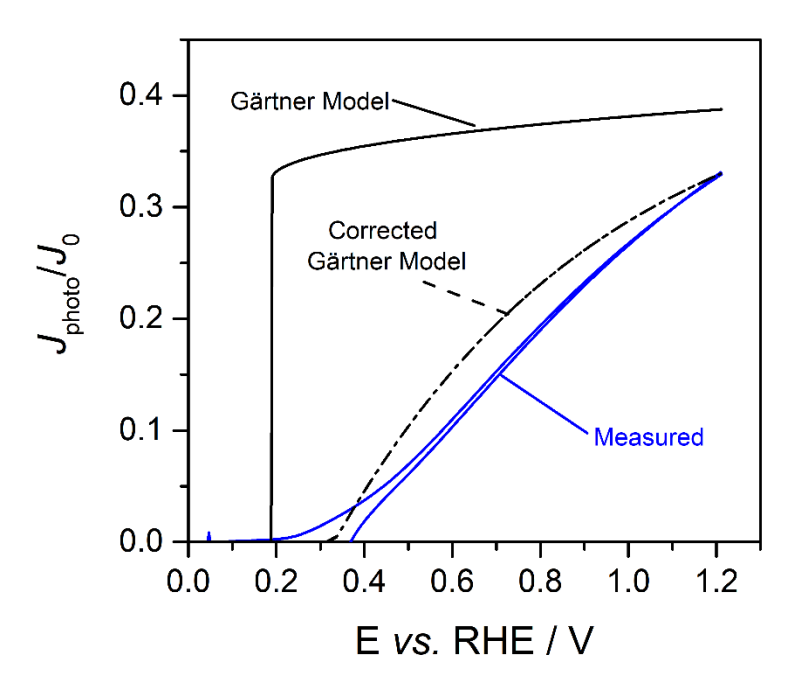


**Figure 9.** The normalized *J-E* curve of Ta<sub>3</sub>N<sub>5</sub> in contact with an aqueous solution containing 0.1 M K<sub>4</sub>[Fe(CN)<sub>6</sub>] as the hole scavenger. A blue LED light with a wavelength of 470 nm (solid line) and an intensity of 4.2 mW cm<sup>-2</sup> was used as the light source. The experimental data is shown in solid blue line, simulated curve using Gärtner model is shown in solid black line, and simulated curve using corrected-Gärtner model for surface charge transfer efficiency is shown in black dashed line. Note: a diffusion length of 50 nm was used in both simulations. Experimental and calculated data for light intensity of 0.81 mW cm<sup>-2</sup> is shown in Figure S28.

We note that the best examples of Ta<sub>3</sub>N<sub>5</sub> electrodes are nanostructured with nanorods, nanotube, and porous cubic morphologies with a diameter/thickness of  $\sim 100$  nm. <sup>1-4,14,57,58</sup> These high aspect ratio electrodes have long been used for various material suffering from limited diffusion length and low absorptivity to maximize their PEC performance by maximizing the light harvesting efficiency while keeping the feature size within the charge collection length, i.e. the distance that minority charge carriers need to travel to reach the surface. <sup>59,60</sup> Interestingly, for Ta<sub>3</sub>N<sub>5</sub> electrodes these feature size are in agreement with the diffusion length of holes estimated by corrected-Gärtner model of our model thin film electrodes. On the other hand, this diffusion length contradicts with the previous study by Van de Krol and coworkers<sup>19</sup> where they predicted that the diffusion length of charge carriers for Ta<sub>3</sub>N<sub>5</sub> is ~ 18,000 nm. They used time-resolved microwave conductivity measurements to analyze charge transport characteristics of Ta<sub>3</sub>N<sub>5</sub>. For preparation of Ta<sub>3</sub>N<sub>5</sub> film they used a two-step procedure consisting of oxidation followed by ammonolysis. First, metallic Ta was sputtered on a fused silica substrate coated with 5 nm Ti. This electrode was then oxidized and nitridized to synthesis Ta<sub>3</sub>N<sub>5</sub> film. We hypothesize that during the oxidation process of the Ta layer, the Ti layer is also oxidized. 61,62 After annealing in ammonia in presence of tantalum oxide the Ti layer forms Tantalum-doped TiO<sub>2</sub> (TTO).<sup>18</sup> We have previously shown that TTO is in fact a transparent conductive substrate. 18 Thus, we speculate that formation of TTO as a conductive substrate can greatly influence their analysis and might be the source of the difference in the calculated diffusion lengths.

## **Conclusions**

In this study, a home-built ALD instrument using a combination of TaCl<sub>5</sub> and ammonia was utilized to directly deposit crystalline Ta<sub>3</sub>N<sub>5</sub> with various thicknesses on various substrates. It was shown that the growth mode (crystallinity, morphology, topography, and growth rate) of Ta<sub>3</sub>N<sub>5</sub> films strongly depend on the number of ALD cycles and the substrate. The variation in growth mode was attributed to the crystal mismatch between substrate and crystalline Ta<sub>3</sub>N<sub>5</sub>. This observation readily opens up a new opportunities to utilize ALD to deposit films of Ta<sub>3</sub>N<sub>5</sub> with controllable crystallographic properties and precise thicknesses by simply modifying the substrate. Furthermore, ALD deposited Ta<sub>3</sub>N<sub>5</sub> films can further be protected *in situ* against photocorrosion with an overlayer of GaN or TiO<sub>2</sub> prior to exposure to the ambient atmosphere. <sup>10,11,63</sup>

Furthermore, it was shown that reducing Ta<sub>3</sub>N<sub>5</sub> synthesis temperature allows the realization of

Ta<sub>3</sub>N<sub>5</sub> on FTO as the state-of-the-art TCO to study the PEC performance of pristine Ta<sub>3</sub>N<sub>5</sub>

independent of the substrate conductivity. Based on the dependency of PEC and EIS analysis and

their dependency on the illumination direction and film thickness, it is clear that the PEC

performance of Ta<sub>3</sub>N<sub>5</sub> is controlled by the diffusion of hole (minority carriers). Using a modified

Gärtner model, we calculated a hole diffusion length of ~ 50 nm which consistent with the best

example of Ta<sub>3</sub>N<sub>5</sub> further indicates that a high aspect ratio nanorods electrode with the feature size

of ~100 nm is probably the optimum electrode architecture to realize a high performing electrode

Ta<sub>3</sub>N<sub>5</sub>. In addition, in high aspect ratio electrode the density of hole at the surface is minimized

which in return can suppress the surface photocorrosion of Ta<sub>3</sub>N<sub>5</sub>.

**Supporting Information** 

detailed description of design and build of ALD; SEM images, AFM analysis, UV-Vis

transmittance and reflectance analysis, XRD, and Raman spectrum, of bare FTO and ALD

deposited Ta<sub>3</sub>N<sub>5</sub> films on FTO substrate; the J-E curves of Ta<sub>3</sub>N<sub>5</sub>|FTO electrode as a

function of illumination direction; spectroscopic ellipsometry characterization of Ta3N5

thin films; photocurrent transient measurement of Ta<sub>3</sub>N<sub>5</sub>|FTO electrode under

monochromatic illumination; list of various methods for thin film synthesis of Ta<sub>3</sub>N<sub>5</sub>;

tabulated values of experimental and calculated physical properties of Ta<sub>3</sub>N<sub>5</sub>.

**Corresponding Author** 

\*E-mail: hamann@chemistry.msu.edu

Acknowledgements

This work was funded by NSF Award CHE-1664823 and the HydroGEN Advanced Water

Splitting Materials Consortium, established as part of the Energy Materials Network under the

U.S. Department of Energy, Office of Energy Efficiency and Renewable Energy, Fuel Cell

Technologies Office Award DE-EE0008086. We also thank Matthew Woodhouse for assistance

with the photoluminescence measurements.

25

### References

- (1) Li, Y.; Zhang, L.; Torres-Pardo, A.; González-Calbet, J. M.; Ma, Y.; Oleynikov, P.; Terasaki, O.; Asahina, S.; Shima, M.; Cha, D.; Zhao, L.; Takanabe, K.; Kubota, J.; Domen, K. Cobalt Phosphate-Modified Barium-Doped Tantalum Nitride Nanorod Photoanode with 1.5% Solar Energy Conversion Efficiency. *Nat. Commun.* 2013, 4, 2566.
- (2) Liu, G.; Ye, S.; Yan, P.; Xiong, F.; Fu, P.; Wang, Z.; Chen, Z.; Shi, J.; Li, C. Enabling an Integrated Tantalum Nitride Photoanode to Approach the Theoretical Photocurrent Limit for Solar Water Splitting. *Energy Environ. Sci.* **2016**, *9* (4), 1327–1334.
- (3) He, Y.; Thorne, J. E.; Wu, C. H.; Ma, P.; Du, C.; Dong, Q.; Guo, J.; Wang, D. What Limits the Performance of Ta<sub>3</sub>N<sub>5</sub> for Solar Water Splitting? *Chem* **2016**, *1* (4), 640–655.
- (4) Cheng, Q.; Fan, W.; He, Y.; Ma, P.; Vanka, S.; Fan, S.; Mi, Z.; Wang, D. Photorechargeable High Voltage Redox Battery Enabled by Ta<sub>3</sub>N<sub>5</sub> and GaN/Si Dual-Photoelectrode. *Adv. Mater.* **2017**, *29* (26), 1700312.
- (5) Dabirian, A.; Van De Krol, R. Resonant Optical Absorption and Defect Control in Ta<sub>3</sub>N<sub>5</sub> Photoanodes. *Appl. Phys. Lett.* **2013**, *102* (3), 033905.
- Yokoyama, D.; Hashiguchi, H.; Maeda, K.; Minegishi, T.; Takata, T.; Abe, R.; Kubota, J.; Domen, K. Ta<sub>3</sub>N<sub>5</sub> Photoanodes for Water Splitting Prepared by Sputtering. *Thin Solid Films* 2011, 519 (7), 2087–2092.
- (7) Cong, Y.; Park, H. S.; Wang, S.; Dang, H. X.; Fan, F. R. F.; Mullins, C. B.; Bard, A. J. Synthesis of Ta<sub>3</sub>N<sub>5</sub> Nanotube Arrays Modified with Electrocatalysts for Photoelectrochemical Water Oxidation. *J. Phys. Chem. C* **2012**, *116* (27), 14541–14550.
- (8) Pei, L.; Lv, B.; Wang, S.; Yu, Z.; Yan, S.; Abe, R.; Zou, Z. Oriented Growth of Sc-Doped Ta<sub>3</sub>N<sub>5</sub> Nanorod Photoanode Achieving Low-Onset-Potential for Photoelectrochemical Water Oxidation. *ACS Appl. Energy Mater.* **2018**, *1* (8), 4150–4157.
- (9) Hara, M.; Chiba, E.; Ishikawa, A.; Takata, T.; Kondo, J. N.; Domen, K. Ta<sub>3</sub>N<sub>5</sub> and TaON Thin Films on Ta Foil: Surface Composition and Stability. *J. Phys. Chem. B* **2003**, *107* (48),

- 13441-13445.
- (10) Zhong, M.; Hisatomi, T.; Sasaki, Y.; Suzuki, S.; Teshima, K.; Nakabayashi, M.; Shibata, N.; Nishiyama, H.; Katayama, M.; Yamada, T.; Domen, K. Highly Active GaN-Stabilized Ta<sub>3</sub>N<sub>5</sub> Thin-Film Photoanode for Solar Water Oxidation. *Angew. Chemie Int. Ed.* 2017, 56 (17), 4739–4743.
- (11) Hu, S.; Shaner, M. R.; Beardslee, J. A.; Lichterman, M.; Brunschwig, B. S.; Lewis, N. S. Amorphous TiO<sub>2</sub> Coatings Stabilize Si, GaAs, and GaP Photoanodes for Efficient Water Oxidation. *Science* (80-. ). **2014**, 344 (6187), 1005–1009.
- (12) Pinaud, B. A.; Vailionis, A.; Jaramillo, T. F. Controlling the Structural and Optical Properties of Ta<sub>3</sub>N<sub>5</sub> Films through Nitridation Temperature and the Nature of the Ta Metal. *Chem. Mater.* **2014**, *26* (4), 1576–1582.
- (13) Dabirian, A.; Van De Krol, R. High-Temperature Ammonolysis of Thin Film Ta<sub>2</sub>O<sub>5</sub> Photoanodes: Evolution of Structural, Optical, and Photoelectrochemical Properties. *Chem. Mater.* **2015**, *27* (3), 708–715.
- (14) Wang, L.; Zhou, X.; Nguyen, N. T.; Hwang, I.; Schmuki, P. Strongly Enhanced Water Splitting Performance of Ta3N5Nanotube Photoanodes with Subnitrides. *Adv. Mater.* **2016**, 28 (12), 2432–2438.
- (15) Higashi, T.; Nishiyama, H.; Suzuki, Y.; Sasaki, Y.; Hisatomi, T.; Katayama, M.; Minegishi, T.; Seki, K.; Yamada, T.; Domen, K. Transparent Ta<sub>3</sub>N<sub>5</sub> Photoanodes for Efficient Oxygen Evolution toward the Development of Tandem Cells. *Angew. Chemie Int. Ed.* **2018**.
- (16) Walter, M. G.; Warren, E. L.; McKone, J. R.; Boettcher, S. W.; Mi, Q.; Santori, E. A.; Lewis, N. S. Solar Water Splitting Cells. *Chem. Rev.* **2010**, *110* (11), 6446–6473.
- (17) Brillet, J.; Comuz, M.; Formal, F. Le; Yum, J. H.; Grätzel, M.; Sivula, K. Examining Architectures of Photoanode-Photovoltaic Tandem Cells for Solar Water Splitting. *J. Mater. Res.* **2010**, *25* (1), 17–24.
- (18) Hajibabaei, H.; Zandi, O.; Hamann, T. W. Tantalum Nitride Films Integrated with

- Transparent Conductive Oxide Substrates: Via Atomic Layer Deposition for Photoelectrochemical Water Splitting. *Chem. Sci.* **2016**, *7* (11), 6760–6767.
- (19) De Respinis, M.; Fravventura, M.; Abdi, F. F.; Schreuders, H.; Savenije, T. J.; Smith, W. A.; Dam, B.; Van De Krol, R. Oxynitrogenography: Controlled Synthesis of Single-Phase Tantalum Oxynitride Photoabsorbers. *Chem. Mater.* **2015**, *27* (20), 7091–7099.
- (20) Henderson, S. J.; Hector, A. L. Structural and Compositional Variations in Ta<sub>3</sub>N<sub>5</sub> Produced by High-Temperature Ammonolysis of Tantalum Oxide. *J. Solid State Chem.* **2006**, *179* (11), 3518–3524.
- (21) Terao, N. Structure of Tantalum Nitrides. *Jpn. J. Appl. Phys.* **1971**, *10* (2), 248–259.
- (22) Ganin, A. Y.; Kienle, L.; Vajenine, G. V. Plasma-Enhanced CVD Synthesis and Structural Characterization of Ta<sub>2</sub>N<sub>3</sub>. *Eur. J. Inorg. Chem.* **2004**, *2004* (16), 3233–3239.
- (23) Hieber, K. Structural and Electrical Properties of Ta and Ta Nitrides Deposited by Chemical Vapour Deposition. *Thin Solid Films* **1974**, *24* (1), 157–164.
- (24) Ritala, M.; Kalsi, P.; Riihelä, D.; Kukli, K.; Leskelä, M.; Jokinen, J. Controlled Growth of TaN, Ta<sub>3</sub>N<sub>5</sub>, and TaO<sub>x</sub>N<sub>y</sub> Thin Films by Atomic Layer Deposition. *Chem. Mater.* **1999**, *11* (7), 1712–1718.
- (25) Hiltunen, L.; Leskelä, M.; Mäkelä, M.; Niinistö, L.; Nykänen, E.; Soininen, P. Nitrides of Titanium, Niobium, Tantalum and Molybdenum Grown as Thin Films by the Atomic Layer Epitaxy Method. *Thin Solid Films* **1988**, *166* (C), 149–154.
- (26) Fang, Z.; Aspinall, H. C.; Odedra, R.; Potter, R. J. Atomic Layer Deposition of TaN and Ta<sub>3</sub>N<sub>5</sub> Using Pentakis(Dimethylamino)Tantalum and Either Ammonia or Monomethylhydrazine. *J. Cryst. Growth* **2011**, *331* (1), 33–39.
- (27) Fix, R.; Gordon, R. G.; Hoffman, D. M. Chemical Vapor Deposition of Vanadium, Niobium, and Tantalum Nitride Thin Films. *Chem. Mater.* **1993**, *5* (5), 614–619.
- (28) Hoffman, D. M. Chemical Vapour Deposition of Nitride Thin Films. *Polyhedron* **1994**, *13*

- (8), 1169-1179.
- (29) Chen, X.; Peterson, G. G.; Goldberg, C.; Nuesca, G.; Frisch, H. L.; Kaloyeros, A. E.; Arkles, B.; Sullivan, J. Low-Temperature Chemical Vapor Deposition of Tantalum Nitride from Tantalum Pentabromide for Integrated Circuitry Copper Metallization Applications. *J. Mater. Res.* 1999, 14 (5), 2043–2052.
- (30) Chiu, H. T.; Chang, W. P. Deposition of Tantalum Nitride Thin Films from Ethylimidotantalum Complex. *J. Mater. Sci. Lett.* **1992**, *11* (2), 96–98.
- (31) Alén, P.; Juppo, M.; Ritala, M.; Sajavaara, T.; Keinonen, J.; Leskelä, M. Atomic Layer Deposition of Ta(Al)N(C) Thin Films Using Trimethylaluminum as a Reducing Agent. *J. Electrochem. Soc.* **2001**, *148* (10), G566–G571.
- (32) Kwon, J. D.; Yun, J.; Kang, S. W. Comparison of Tantalum Nitride Films for Different NH<sub>3</sub>/H<sub>2</sub>/Ar Reactant States in Two-Step Atomic Layer Deposition. *Jpn. J. Appl. Phys.* **2009**, 48 (2), 025504.
- (33) Schneider, C. A.; Rasband, W. S.; Eliceiri, K. W. NIH Image to ImageJ: 25 Years of Image Analysis. *Nat. Methods* **2012**, *9* (7), 671–675.
- (34) Klahr, B. M.; Martinson, A. B. F.; Hamann, T. W. Photoelectrochemical Investigation of Ultrathin Film Iron Oxide Solar Cells Prepared by Atomic Layer Deposition. *Langmuir* **2011**, *27* (1), 461–468.
- (35) Ziani, A.; Nurlaela, E.; Dhawale, D. S.; Silva, D. A.; Alarousu, E.; Mohammed, O. F.; Takanabe, K. Carrier Dynamics of a Visible-Light-Responsive Ta<sub>3</sub>N<sub>5</sub> Photoanode for Water Oxidation. *Phys. Chem. Chem. Phys.* **2015**, *17* (4), 2670–2677.
- (36) Morbec, J. M.; Narkeviciute, I.; Jaramillo, T. F.; Galli, G. Optoelectronic Properties of Ta<sub>3</sub>N<sub>5</sub>: A Joint Theoretical and Experimental Study. *Phys. Rev. B Condens. Matter Mater. Phys.* **2014**, *90* (15), 155204.
- (37) Chun, W. J.; Ishikawa, A.; Fujisawa, H.; Takata, T.; Kondo, J. N.; Hara, M.; Kawai, M.; Matsumoto, Y.; Domen, K. Conduction and Valence Band Positions of Ta<sub>2</sub>O<sub>5</sub>, TaON, and

- Ta<sub>3</sub>N<sub>5</sub> by UPS and Electrochemical Methods. *J. Phys. Chem. B* **2003**, *107* (8), 1798–1803.
- (38) Nurlaela, E.; Ould-Chikh, S.; Harb, M.; Del Gobbo, S.; Aouine, M.; Puzenat, E.; Sautet, P.; Domen, K.; Basset, J. M.; Takanabe, K. Critical Role of the Semiconductor-Electrolyte Interface in Photocatalytic Performance for Water-Splitting Reactions Using Ta<sub>3</sub>N<sub>5</sub> Particles. *Chem. Mater.* **2014**, *26* (16), 4812–4825.
- (39) Maeda, K.; Terashima, H.; Kase, K.; Higashi, M.; Tabata, M.; Domen, K. Surface Modification of TaON with Monoclinic ZrO<sub>2</sub> to Produce a Composite Photocatalyst with Enhanced Hydrogen Evolution Activity under Visible Light. *Bull. Chem. Soc. Jpn.* **2008**, 81 (8), 927–937.
- (40) Yuliati, L.; Yang, J. H.; Wang, X.; Maeda, K.; Takata, T.; Antonietti, M.; Domen, K. Highly Active Tantalum(v) Nitride Nanoparticles Prepared from a Mesoporous Carbon Nitride Template for Photocatalytic Hydrogen Evolution under Visible Light Irradiation. *J. Mater. Chem.* **2010**, *20* (21), 4295–4298.
- (41) Fu, G.; Yan, S.; Yu, T.; Zou, Z. Oxygen Related Recombination Defects in Ta<sub>3</sub>N<sub>5</sub> Water Splitting Photoanode. *Appl. Phys. Lett.* **2015**, *107* (17), 171902.
- (42) Brese, N. E.; O'Keeffe, M.; Rauch, P.; DiSalvo, F. J. Structure of Ta<sub>3</sub>N<sub>5</sub> at 16 K by Time-of-Flight Neutron Diffraction. *Acta Crystallogr. Sect. C Cryst. Struct. Commun.* **1991**, 47 (11), 2291–2294.
- (43) Higashi, M.; Domen, K.; Abe, R. Fabrication of Efficient TaON and Ta<sub>3</sub>N<sub>5</sub> Photoanodes for Water Splitting under Visible Light Irradiation. *Energy Environ. Sci.* **2011**, *4* (10), 4138–4147.
- (44) Narkeviciute, I.; Chakthranont, P.; MacKus, A. J. M.; Hahn, C.; Pinaud, B. A.; Bent, S. F.; Jaramillo, T. F. Tandem Core-Shell Si-Ta<sub>3</sub>N<sub>5</sub> Photoanodes for Photoelectrochemical Water Splitting. *Nano Lett.* **2016**, *16* (12), 7565–7572.
- (45) Pinaud, B. A.; Vesborg, P. C. K.; Jaramillo, T. F. Effect of Film Morphology and Thickness on Charge Transport in Ta<sub>3</sub>N<sub>5</sub>/Ta Photoanodes for Solar Water Splitting. *J. Phys. Chem. C* **2012**, *116* (30), 15918–15924.

- (46) Cohen, S. R.; Plane, R. A. The Association of Ferrocyanide Ions with Various Cations. *J. Phys. Chem.* **1957**, *61* (8), 1096–1100.
- (47) Gelderman, K.; Lee, L.; Donne, S. W. Flat-Band Potential of a Semiconductor: Using the Mott–Schottky Equation. *J. Chem. Educ.* **2007**, *84* (4), 685–688.
- (48) Nurlaela, E.; Harb, M.; Del Gobbo, S.; Vashishta, M.; Takanabe, K. Combined Experimental and Theoretical Assessments of the Lattice Dynamics and Optoelectronics of TaON and Ta<sub>3</sub>N<sub>5</sub>. *J. Solid State Chem.* **2015**, *229*, 219–227.
- (49) Khan, S.; Zapata, M. J. M.; Pereira, M. B.; Gonçalves, R. V.; Strizik, L.; Dupont, J.; Santos,
  M. J. L.; Teixeira, S. R. Structural, Optical and Photoelectrochemical Characterizations of
  Monoclinic Ta<sub>3</sub>N<sub>5</sub> Thin Films. *Phys. Chem. Chem. Phys.* 2015, 17 (37), 23952–23962.
- (50) Gärtner, W. W. Depletion-Layer Photoeffects in Semiconductors. *Phys. Rev.* **1959**, *116* (1), 84–87.
- (51) Butler, M. A. Photoelectrolysis and Physical Properties of the Semiconducting Electrode WO2. *J. Appl. Phys.* **1977**, *48* (5), 1914–1920.
- (52) Thorne, J. E.; Jang, J. W.; Liu, E. Y.; Wang, D. Understanding the Origin of Photoelectrode Performance Enhancement by Probing Surface Kinetics. *Chem. Sci.* **2016**, *7* (5), 3347–3354.
- (53) Iwanski, P. The Photoelectrochemical Behavior of Ferric Oxide in the Presence of Redox Reagents. *J. Electrochem. Soc.* **1981**, *128* (10), 2128–2133.
- (54) Abrantes, L. M.; Peter, L. M. Transient Photocurrents at Passive Iron Electrodes. *J. Electroanal. Chem. Interfacial Electrochem.* **1983**, *150* (1–2), 593–601.
- (55) Peter, L. M.; Wijayantha, K. G. U.; Tahir, A. A. Kinetics of Light-Driven Oxygen Evolution at α-Fe<sub>2</sub>O<sub>3</sub> Electrodes. *Faraday Discuss.* **2012**, *155* (0), 309–322.
- (56) Hajibabaei, H.; Gao, Y.; Hamann, T. W. Chapter 4: Unravelling the Charge Transfer Mechanism in Water Splitting Hematite Photoanodes. In *RSC Energy and Environment*

- Series; S David Tilley, Stephan Lany, R. van de K., Ed.; 2018; Vol. 2018–Janua, pp 100–127.
- (57) Li, Y.; Takata, T.; Cha, D.; Takanabe, K.; Minegishi, T.; Kubota, J.; Domen, K. Vertically Aligned Ta<sub>3</sub>N<sub>5</sub> Nanorod Arrays for Solar-Driven Photoelectrochemical Water Splitting. *Adv. Mater.* **2013**, *25* (1), 125–131.
- (58) Narkeviciute, I.; Jaramillo, T. F. Impact of Nanostructuring on the Photoelectrochemical Performance of Si/Ta 3 N 5 Nanowire Photoanodes. *J. Phys. Chem. C* **2017**, *121* (49), 27295–27302.
- (59) Sivula, K.; Le Formal, F.; Grätzel, M. Solar Water Splitting: Progress Using Hematite (α-Fe<sub>2</sub>O<sub>3</sub>) Photoelectrodes. *ChemSusChem* **2011**, *4* (4), 432–449.
- (60) Cesar, I.; Sivula, K.; Kay, A.; Zboril, R.; Grätzel, M. Influence of Feature Size, Film Thickness, and Silicon Doping on the Performance of Nanostructured Hematite Photoanodes for Solar Water Splitting. *J. Phys. Chem. C* **2009**, *113* (2), 772–782.
- (61) Narushima, T.; Sado, S.; Kondo, N.; Ueda, K.; Kawano, M.; Ogasawara, K. Evaluation of Photocatalytic Activity of the TiO<sub>2</sub> Layer Formed on Ti by Thermal Oxidation. In *Interface Oral Health Science 2014*; Springer Japan: Tokyo, 2015; pp 65–78.
- (62) Lee, K. S.; Park, I. S. Anatase-Phase Titanium Oxide by Low Temperature Oxidation of Metallic Ti Thin Film. *Scr. Mater.* **2003**, *48* (6), 659–663.
- (63) McDowell, M. T.; Lichterman, M. F.; Spurgeon, J. M.; Hu, S.; Sharp, I. D.; Brunschwig, B. S.; Lewis, N. S. Improved Stability of Polycrystalline Bismuth Vanadate Photoanodes by Use of Dual-Layer Thin TiO<sub>2</sub>/Ni Coatings. *J. Phys. Chem. C* 2014, 118 (34), 19618–19624.

# TOC Graphic

